Proceedings of CONF-FMCE 2026 Symposium: Smart City and Infrastructure Engineering
DOI: 10.54254/2755-2721/2026.CH38770

Design of Residential Photovoltaic Power Generation Systems for Low-Carbon Buildings

Chenxi Zhang

Shanghai United International School Gubei Campus, Shanghai, China
zhangchenxi081116@163.com

Abstract. Decarbonising residential buildings is a combination of energy demand reduction on the demand side and renewable electricity generation on the supply side. In Shanghai, rooftop photovoltaic (PV) generation could be a viable option to reduce household electric power consumption for detached residential buildings, provided PV array sizing, design of power conversion, grid-filtering and control strategy are tailored. In this paper a preliminary electrical design of a grid connected PV power generation system is based on the low carbon residential building to provide the annual electricity balance is developed. Given a winter design demand of 17.8 kWh/day, an effective sunshine duration of 3.8 h/day and a system-loss coefficient of 1.8, the PV capacity is found to be 8.43 kW. A 10.08 kWp array is selected for use, which consists of 24 mono-crystalline silicon modules, and an estimated module area of 48.0m2. The design is also specified by the direct current (DC) bus voltage of 400 V, the frequency of the DC-DC boost converter of 10 kHz, the frequency of the single-phase sinusoidal pulse-width modulation (SPWM) inverter of 20 kHz, and an inductor-capacitor-inductor (LCL) grid filter. A hybrid constant-voltage and perturb-and-observe maximum power point tracking (MPPT) strategy is employed to enhance the PV operating point tracking under the condition of irradiance change. The simulation results reveal that the hybrid MPPT controller is able to track the new MPP following an irradiance drop from 1200 W/m2 to 600 W/m2 at t=0.8 s. Capacitor current feedback active damping for the LCL filter suppresses the resonance peak and the grid current total harmonic distortion is less than the design limit of 5.00% at 2.45%. These results are helpful for electrical feasibility of the proposed grid connected residential PV system.

Keywords: low-carbon building, photovoltaic power generation system, maximum power point tracking, LCL filter, harmonic suppression

1. Introduction

A major opportunity for decarbonisation of carbon emissions from buildings' operation is the decarbonisation of residential buildings, as they represent a significant percentage of the global energy demand and energy-related carbon emissions. Efficiency improvement on the building side and integration of renewable energies are needed for low-carbon development; in 2022, the global building and construction industry consumed about 34% of the energy and generated around 37% of energy- and process-related CO_2 emissions. The policy goal of China's carbon neutrality before 2060

© 2026 The Authors. This is an open access article distributed under the terms of the Creative Commons Attribution License 4.0 (https://creativecommons.org/licenses/by/4.0/).

DOI: 10.54254/2755-2721/2026.CH38770

and peaking carbon dioxide (CO_2) emissions before 2030 also reinforces the need to decrease the operational CO_2 emissions from the residential sector [1, 2].

Residential buildings are chosen as the object of study as their electric power consumption is very closely related to daily life activities like air conditioning, lighting, refrigeration, cooking and appliances in the households. Past research on decarbonisation of residential buildings in China has indicated that the measures to be taken for moving towards the long-term carbon neutral operation of a building include reducing energy intensity of end-uses and promoting BIPV and BAPV renewable energy generation [3]. Hence, this paper investigates a residential scale PV system, not only as a stand-alone power-electronic device but also within the framework of a building-level operational energy-balance strategy.

Shanghai is chosen as the case-study region, for three reasons. Firstly it lies in the hot summer, cold winter climatic zone, where air-conditioning load, as a residential load, plays a significant role in determining the electricity demand. Secondly, Shanghai has practical experience of building-attached PV systems; it was found that monitored rooftop Building Attached Photovoltaic (BAPV) operation in Shanghai indicates the integration of residential rooftop PV systems in local buildings and their grid connection [4-6]. Third, Shanghai is a high-density urban area, and has a large distributed-energy demand, making it a representative test area for the study of the effect of rooftop PV generation in reducing household electricity consumption. With this background, the following design is based on a representative case, a detached multigenerational residential dwelling in Shanghai, to relate the electrical design assumptions to the end-use demand, the air-conditioning load of the selected dwelling and the feasibility of PV installation on the roof. This specific research question is thus raised in this paper: What implementation and design of passive energy-efficiency measures and PVs can be mutually developed and assessed to enable annual operational electricity balance for a detached house in the Shanghai region?

The reduced design electricity demand that was used as input in PV sizing represents the passive measures in this preliminary study. This work does not account for detailed thermal modelling of the building envelope, embodied emissions of the construction materials, and full life cycle carbon accounting. The PV capacity required to meet the demand on the design day is computed as the first step of the method and the effective sunshine duration is obtained from the local weather conditions. It then details the PV array, direct-current (DC) converter, DC bus, single-phase inverter, and LCL filter. Finally, a hybrid maximum-power-point-tracking (MPPT) method and capacitor-current-feedback (CCF) active damping for the grid interface are proposed. The annual electricity balance is not considered a full low-carbon certification and thus the final design must be checked against measured or simulated annual loads and irradiation data.

2. System architecture and design basis

Figure 1 shows the proposed grid-connected residential PV architecture. The PV array supplies a DC-DC boost converter, which raises and regulates the array voltage at the 400 V DC bus. A single-phase DC-AC inverter converts this DC power to AC power. The LCL filter suppresses high-frequency switching harmonics before the inverter output is connected to the utility grid and household loads through a bidirectional meter. The bidirectional meter records grid imports and exports, which are required for subsequent annual-energy-balance validation [7-9].

Consistent with the research scope established in Section I, the case object is defined as a detached residential dwelling in Shanghai. A residential building is selected because operational residential-building decarbonization in China depends strongly on reducing end-use electricity demand and increasing the contribution of building-integrated or building-applied renewable

DOI: 10.54254/2755-2721/2026.CH38770

electricity [3]. Shanghai is selected because building-scale solar-energy assessment is particularly relevant in dense urban regions, where rooftop area, surrounding obstruction, and seasonal solar-radiation variation directly affect PV feasibility [4-6]. The dwelling is therefore modelled as a large multigenerational residential design case with a floor area of approximately 150 m^2. This floor area is used as a case-study assumption rather than as a statistical average. The winter design demand is taken as $Q = 17.8\ \mathrm{kWh/day}$, based on the assumed load inventory of air-conditioning, lighting, refrigeration, cooking, and household appliances. The effective winter sunshine duration is set as $T_m = 3.8\ \mathrm{h/day}$, which should be obtained from site-specific solar-irradiation data for Shanghai. The system-loss coefficient $K_s = 1.8$ is adopted as a conservative preliminary design factor to include temperature loss, soiling, wiring loss, mismatch, inverter/converter loss, and operational uncertainty [10]. Each PV module is specified as 0.42 kW, with $V_{\mathrm{mp}} = 32.6$ V, $I_{\mathrm{mp}} = 13.14$ A, $V_{\mathrm{oc}} = 38.46$ V, and $I_{\mathrm{sc}} = 14.09$ A. Assuming a mono-crystalline module efficiency of approximately 21%, each module requires an active area of about 2.00 m^2, so the 24-module array requires a total module area of approximately 48.0 m^2. A practical rooftop area of approximately 55–60 m^2 should be reserved to allow for mounting gaps, edge clearance, and maintenance access. The converter design uses Udc = 400 V, Pb = 10 kW, a 10 kHz boost switching frequency, and a 20 kHz inverter switching frequency. The grid interface is specified as 220 V RMS at 50 Hz, consistent with China's low-voltage single-phase supply and nominal AC frequency requirements [11].

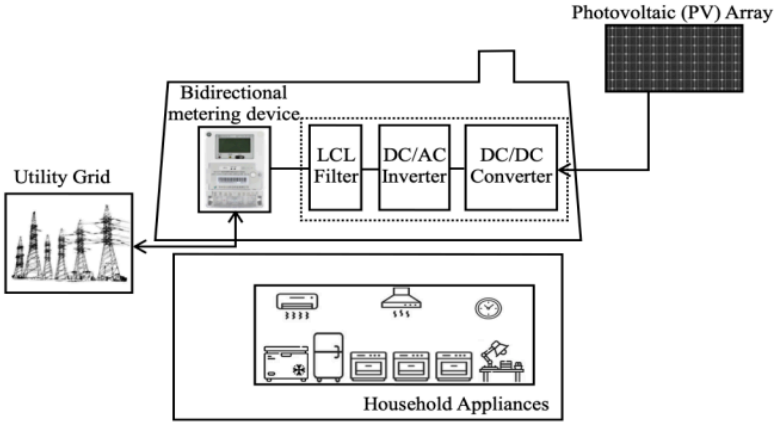

Figure 1. Grid-connected residential PV system architecture

2.1. PV array sizing and configuration

The PV array is sized from the daily electrical energy requirement rather than from instantaneous power alone. The minimum nominal PV capacity is calculated using the design-day demand Q, the system-loss coefficient Ks, and the effective sunshine duration Tm

$$P_{PV,min} = \frac{QK_s}{T_m} \tag{1}$$

where Q is the estimated winter daily electricity demand, Ks represents aggregate losses due to factors such as temperature, soiling, wiring, converter losses, and operational uncertainty, and Tm is the average effective sunshine duration in winter. The required number of PV modules is therefore

$$N_{min} = \left\lceil \frac{P_{PV,min}}{P_s} \right\rceil \tag{2}$$

DOI: 10.54254/2755-2721/2026.CH38770

Because the calculated value is 20.07 before rounding, a 20-module array would be marginally below the stated 8.43 kW requirement. To preserve an equal number of modules in every series string and to provide an engineering margin compatible with the 10 kW power stage, this revised design selects 24 modules. The resulting nominal installed capacity is 24 × 0.42 = 10.08 kWp.

The selected 24 modules are arranged as four modules in series per string and six strings in parallel. This configuration gives $V_{\mathrm{PV,mp}} = 4V_{\mathrm{mp}} = 130.4$ V and $I_{\mathrm{PV,mp}} = 6I_{\mathrm{mp}} = 78.84$ A, which provide the input condition for the boost-converter design. The corresponding open-circuit voltage and short-circuit current are $V_{\mathrm{PV,oc}} = 153.84$ V and $I_{\mathrm{PV,sc}} = 84.54$ A, respectively.

2.2. DC-DC boost converter

The boost converter used to raise the PV-array voltage to the DC-bus voltage while allowing the controller to regulate the operating point of the PV array. For an ideal boost converter operating in continuous-conduction mode, the voltage and current relationships are

$$\frac{U_{dc}}{U_{pv}} = \frac{1}{1-D}, \tag{3}$$

$$\frac{I_{dc}}{I_{pv}} = 1 - D, \tag{4}$$

where U_{pv} and I_{pv} are the PV-side voltage and current, U_{dc} and I_{dc} are the DC-bus voltage and current, and D is the switch duty ratio. The PV-side effective load resistance is consequently

$$R_{in} = \frac{U_{pv}}{I_{pv}} = R_L(1-D)^2, \qquad R_L = \frac{U_{dc}}{I_{dc}}. \tag{5}$$

Equation (5) is important for MPPT: changing D changes the effective resistance seen by the PV array and therefore moves its electrical operating point. It should not be interpreted as a fixed physical internal resistance of the PV cells (see Figure 2).

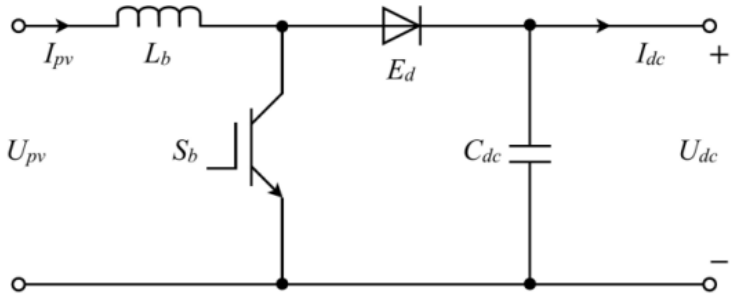

Figure 2. Boost-converter topology

At the array maximum-power-point voltage of 130.4 V and the 400 V DC-bus voltage, the ideal duty ratio is D = 1 − 130.4/400 = 0.674. If the peak-to-peak inductor-current ripple is limited to $\eta = 18\%$ of the average PV-side current, the minimum inductance is

$$L_b = \frac{D(1-D)^2 U_{dc}^2}{\eta P_b f_b}. \tag{6}$$

DOI: 10.54254/2755-2721/2026.CH38770

In Equation (6), Lb is the boost inductance, Pb is the rated converter power, and fb is the boost switching frequency. A value of 0.70 mH is selected to provide margin. At 10 kW, the average PV-side current is Pb/Upv = 76.7 A. With 18% peak-to-peak ripple, the approximate peak switch current is 83.6 A. An 800 V, 120 A IGBT and an 800 V, 120 A diode therefore provide appropriate nominal voltage and current margin for this preliminary design.

2.3. DC-bus capacitor and single-phase inverter

The DC-bus capacitor limits the low-frequency voltage ripple caused by the single-phase power transfer. With a permissible ripple coefficient $\lambda = 6\%$, the required capacitance is

$$C_{dc} = \frac{P_b}{4\lambda f_0 U_{dc}^2} \tag{7}$$

where, C_{dc} is the DC-bus capacitance and $f_0 = 50$ Hz is the grid frequency. A rated capacitance of at least 6.0 mF should therefore be selected; the previously stated 4.5 mF value does not provide the intended margin under the stated 10 kW design condition.

The inverter is a single-phase full bridge using sinusoidal pulse-width modulation (SPWM), as shown in Figure 3. It operates at fsw = 20 kHz and provides a 220 V RMS, 50 Hz AC output for grid connection. For a 10 kW output, the RMS grid current and the corresponding sinusoidal peak current are

$$I_{ac,rms} = \frac{P_b}{U_g}, \qquad I_{ac,pk} = \sqrt{2} I_{ac,rms} \tag{8}$$

The maximum blocking voltage of each inverter IGBT is approximately the 400 V DC-bus voltage. IGBTs rated at 800 V and 80 A are therefore selected as a preliminary choice, subject to final thermal and switching-loss verification (see Figure 3).

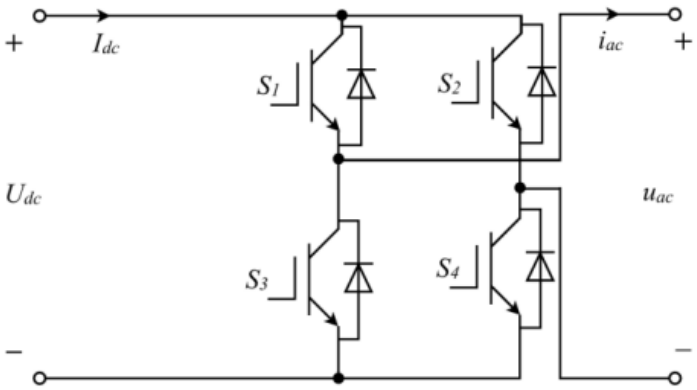

Figure 3. DC-AC inverter

2.4. LCL filter design

An LCL filter is used at the inverter output because it provides stronger high-frequency attenuation than an L filter while using relatively modest inductance. Figure 4 defines the inverter-side inductor L1, grid-side inductor L2, filter capacitor C, inverter-side current iac, capacitor current ic, and grid voltage ug.

DOI: 10.54254/2755-2721/2026.CH38770

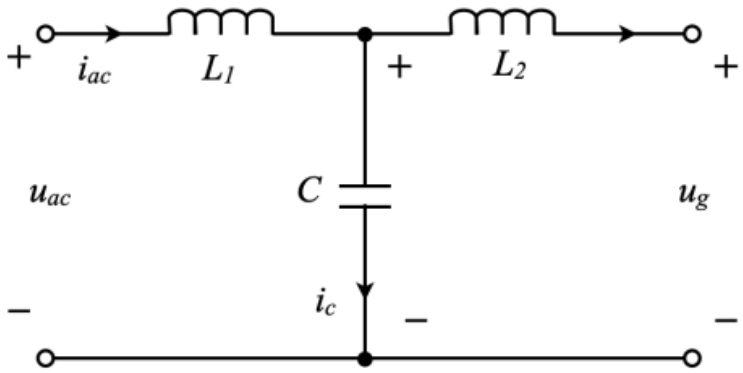

Figure 4. LCL filter connected between the inverter and utility grid

The minimum inverter-side inductance is estimated from the allowable switching-current ripple

$$L_1 \geq \frac{U_{dc}}{4 f_{sw} I_{pm}}, \qquad I_{pm} = 0.20 I_{ac,pk}. \tag{9}$$

In Equation (9), Ipm is the permissible harmonic-current peak, selected as 20% of the rated current peak. The filter-capacitor reactive power is limited to 5% of the rated power, giving

$$C_{max} = \frac{0.05 P_b}{2\pi f_0 U_g^2}. \tag{10}$$

A practical preliminary selection is $L_1 = 0.50$ mH, $L_2 = 0.30$ mH, and C = 16. 0 uF. This gives $L_2/L_1 = 0.60$, maintains the fundamental-frequency voltage drop below 10% of U_g, and keeps capacitor reactive power below the 5% limit. The resonant frequency is

$$f_r = \frac{1}{2\pi}\sqrt{\frac{L_1 + L_2}{L_1 L_2 C}} \tag{11}$$

which lies above the 50 Hz grid frequency and below half of the 20 kHz switching frequency. Under ideal component assumptions, the LCL-filter transfer function is

$$G_{LCL}(s) = \frac{I_g(s)}{U_{ac}(s)} = \frac{1}{L_1 L_2 C s^3 + (L_1 + L_2)s} \tag{12}$$

3. Control-system strategy design

3.1. Hybrid constant-voltage and perturb-and-observe MPPT

The PV array has a nonlinear current-voltage characteristic and a corresponding power-voltage curve. Under uniform irradiance, the power-voltage curve has one maximum-power point. Irradiance and cell temperature shift this point because they change the PV current-voltage characteristic. The boost converter can respond by changing the duty ratio D , which changes the effective input resistance in Equation (5) and moves the PV operating point. Under partial shading, multiple local maxima may occur; therefore, the present constant-voltage plus perturb-and-observe method assumes shading is limited or that a separate global-MPPT method is added [11].

Figure 5 combines the two stages of the MPPT strategy. During startup, the controller estimates the open-circuit voltage Uoc and sets a reference voltage Uref $= 0.78\ U_{oc}$. This constant-voltage

DOI: 10.54254/2755-2721/2026.CH38770

stage provides a rapid approach to the expected maximum-power region. Once |Upv-Uref| is below a specified threshold ϵ, the controller switches to perturb-and-observe tracking. At sampling instant k, it calculates P(k) = Upv(k)Ipv(k) and uses the signs of ΔP=P(k)-P(k-1) and ΔU=U(k) - U(k - 1) to continue or reverse the voltage perturbation. A small perturbation step improves steady-state accuracy but slows response to rapid environmental changes.

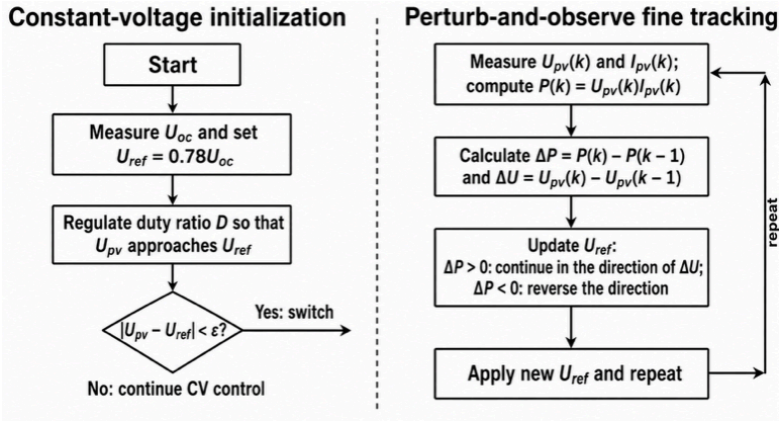

Figure 5. Hybrid MPPT algorithm combining constant-voltage initialization and perturb-and-observe fine tracking

3.2. LCL resonance suppression by capacitor-current feedback

The LCL filter can introduce a resonant peak that reduces grid-current stability if it is not damped [9, 12]. Figure 6 shows capacitor-current-feedback active damping. In the model, $A(s)$ is the current-controller input, a_{PWM} is the inverter modulation gain, $I_g(s)$ is the grid current, and $I_c(s)$ is the capacitor current. For the idealized third-order model, the closed-loop transfer relation is

$$\frac{I_g(s)}{A(s)} = \frac{aa_{PWM}}{L_1L_2Cs^3+aa_{PWM}L_2Cs^2+(L_1+L_2)s}. \tag{13}$$

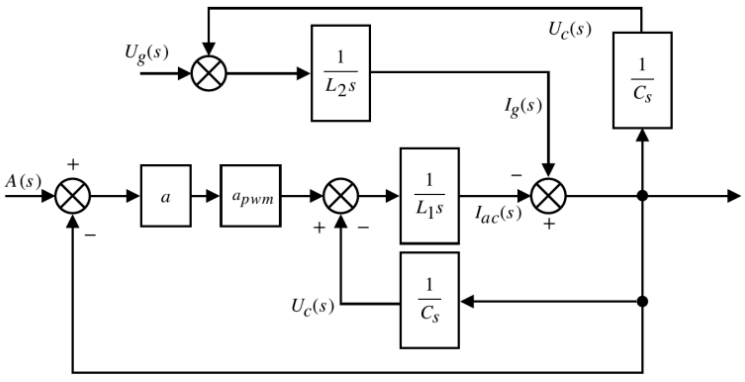

Figure 6. Capacitor-current-feedback active damping for LCL resonance suppression

Resonance suppression is required because the LCL filter introduces a third-order resonance peak between the grid frequency and the inverter switching frequency. If this peak is not damped, small disturbances, sampling delay, or grid-impedance variation may amplify the grid current and reduce system stability. Capacitor-current-feedback active damping is used because it emulates a damping effect without adding a physical resistor, thereby avoiding additional power loss. By feeding back

DOI: 10.54254/2755-2721/2026.CH38770

the filter-capacitor current to the inverter control loop, the resonance peak can be attenuated while maintaining the high-frequency harmonic attenuation advantage of the LCL filter [13, 14].

The damping ratio can be expressed as:

$$\zeta = \frac{aa_{PWM}}{2}\sqrt{\frac{L_2C}{L_1(L_1+L_2)}}. \tag{14}$$

For a nominal damping ratio of $\zeta = 1/\sqrt{2} \approx 0.707$, $a_{PWM} = 400$, and the LCL values selected above, the capacitor-current proportional coefficient is $a \approx 0.041$. This is a model-based initial setting; the final value must be confirmed through simulation and hardware tests because parasitic resistances, sampling delay, and grid-impedance variation affect the actual damping response [13, 14].

4. Simulation verification

4.1. MPPT response under irradiance step change

Based on the design of the main circuit and control strategy, a simulation model of the complete photovoltaic power generation system was built in Simulink. During the simulation, the irradiance was set to 1200 $\mathrm{W/m^2}$, the ambient temperature was set to 25°C, and the household appliances were represented by an 8 Ω resistor with a power of xx kW. In addition, to analyse the influence of irradiance variation on the power generation system, the irradiance of the photovoltaic array module was set to decrease from 1200 $\mathrm{W/m^2}$ to 600 $\mathrm{W/m^2}$ at $t = 0.8$ s .

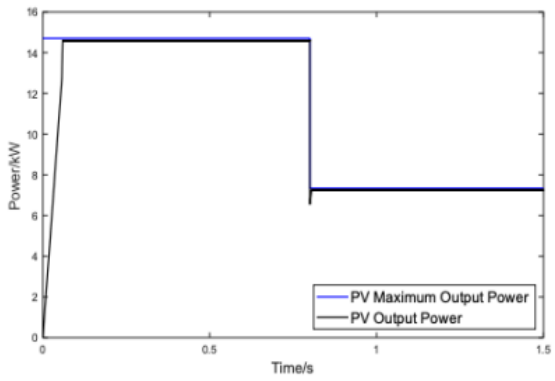

Figure 7. PV output power response under an irradiance step change

Figure 7 shows the output power curve of the photovoltaic array. It can be observed that, during system start-up, the output power of the photovoltaic array is initially low. However, under the constant-voltage plus perturb-and-observe control strategy, the output power rises rapidly and reaches the maximum power point. At $t = 0.8$ s, when the irradiance decreases from 1200 $\mathrm{W/m^2}$ to 600 $\mathrm{W/m^2}$, the system is still able to rapidly track the corresponding new maximum power point. This verifies the effectiveness of the MPPT control strategy adopted in this design.

4.2. LCL resonance suppression result

Figure 8 shows the magnitude-frequency characteristic curves of the modified LCL filter and the original LCL filter. It can be observed that, through capacitor-current-feedback damping, the

DOI: 10.54254/2755-2721/2026.CH38770

resonance peak is significantly suppressed, indicating an effective resonance-suppression performance.

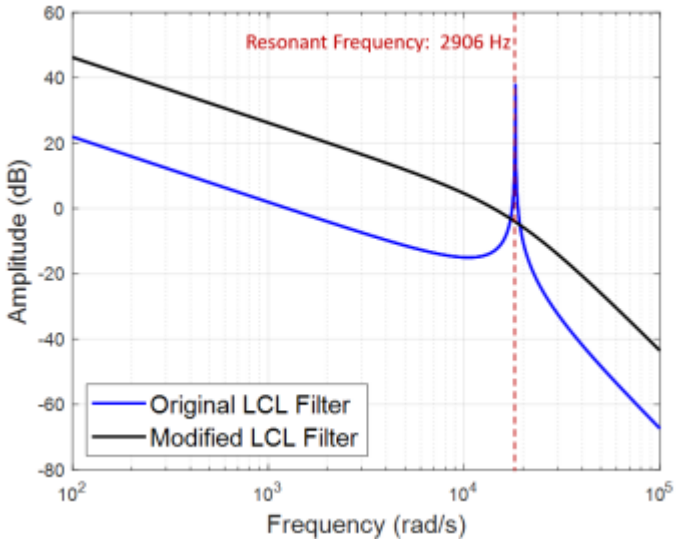

Figure 8. Magnitude-frequency response comparison of the original LCL filter and the modified LCL filter with capacitor-current-feedback damping

4.3. Grid-current harmonic analysis

Figure 9 shows the harmonic analysis result of the grid-connected output current of the photovoltaic system. It can be seen from the figure that the total harmonic distortion (THD) of the current is 2.45% , which is lower than the 5.00% limit required by the national standard. Therefore, the power quality satisfies the grid-connection requirements for photovoltaic systems.

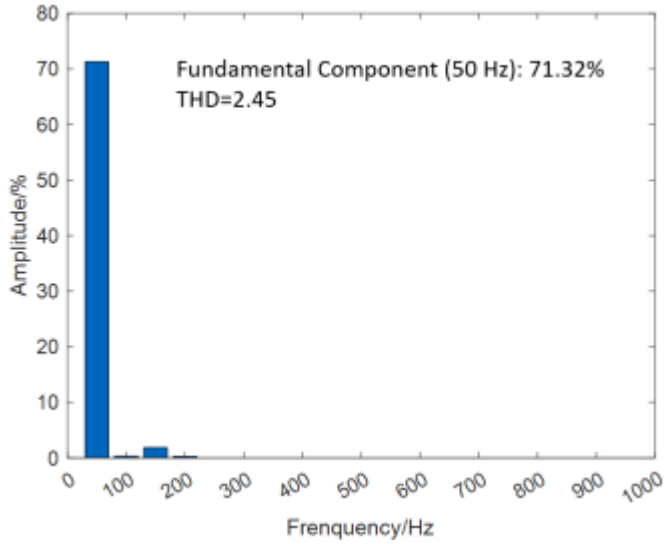

Figure 9. Harmonic spectrum of the grid-connected output current

DOI: 10.54254/2755-2721/2026.CH38770

5. Annual-energy-balance evaluation

The electrical design above specifies the PV and power-conversion system but does not, by itself, prove annual energy balance. The annual operational balance should be evaluated using

$$B_{ann} = E_{PV,ann} - E_{load,ann}, \tag{15}$$

where $E_{\mathrm{PV,ann}}$ is the annual PV generation and $E_{\mathrm{load,ann}}$ is the annual building electricity consumption after passive energy-efficiency measures. A non-negative B_{ann} indicates annual operational electricity balance under the assumed grid-export arrangement.

The simulation results verify the proposed control and filtering strategies. Under an irradiance step from $1200\ \mathrm{W/m^2}$ to $600\ \mathrm{W/m^2}$ at $t = 0.8$ s, the hybrid MPPT controller rapidly tracks the new maximum-power point. The frequency-domain simulation shows that capacitor-current-feedback damping suppresses the LCL-filter resonance peak, and the grid-current THD is 2.45%, below the 5.00% design limit.

6. Conclusion

This paper proposes a design for a grid-connected photovoltaic system for a multi-story detached residence in the Shanghai area. Simulation results indicate that the proposed system demonstrates preliminary feasibility in terms of photovoltaic energy harvesting, grid interface filtering, and harmonic suppression. Following research will utilize actual household electricity consumption data to verify the system's effectiveness in energy conservation and emissions reduction. Based on measured or simulated data for building loads and solar irradiance over the 12 months of the year, the annual power balance is further verified using the equation B_ann = E_PV,ann − E_load,ann, to confirm the system's carbon reduction potential under real-world operating conditions.

References

[1] National Development and Reform Commission of the People's Republic of China. (2021). Action plan for carbon dioxide peaking before 2030.

[2] United Nations Environment Programme. (2024). *Global status report for buildings and construction*. UNEP.

[3] Zou, C., Ma, M., Zhou, N., Feng, W., You, K., & Zhang, S. (2023). Toward carbon free by 2060: A decarbonization roadmap of operational residential buildings in China. *Energy, 277*, 127689. https://doi.org/10.1016/j.energy.2023.127689

[4] Zhang, Z., Chen, M., Zhong, T., et al. (2023). Carbon mitigation potential afforded by rooftop photovoltaic in China. *Nature Communications, 14*, Article 2347. https://doi.org/10.1038/s41467-023-38079-3

[5] Chen, Z., Yu, B., Li, Y., Wu, Q., et al. (2022). Assessing the potential and utilization of solar energy at the building-scale in Shanghai. *Sustainable Cities and Society, 82*, 103917. https://doi.org/10.1016/j.scs.2022.103917

[6] Ni, H., Wang, D., Zhao, W., Jiang, W., Mingze, E., Huang, C., & Yao, J. (2024). Enhancing rooftop solar energy potential evaluation in high-density cities: A deep learning and GIS based approach. *Energy and Buildings, 309*, 113743. https://doi.org/10.1016/j.enbuild.2023.113743

[7] Benabdelkader, A., Draou, A., AlKassem, A., Toumi, T., Denai, M., Abdelkhalek, O., & Ben Slimene, M. (2023). Enhanced power quality in single-phase grid-connected photovoltaic systems: An experimental study. *Energies, 16*(10), 4240. https://doi.org/10.3390/en16104240

[8] Hosseinpour, M., Sabetfar, T., Dejamkhooy, A., & Shahparasti, M. (2023). Design and control of LCL-type grid-tied PV power conditioning system based on inverter and grid side currents double feedback. *International Journal of Modelling and Simulation*. https://doi.org/10.1080/02286203.2023.2204319

[9] Hollweg, G. V., Khan, S. A., Chaturvedi, S., Fan, Y., Wang, M., Su, W., et al. (2023). Grid-connected converters: A brief survey of topologies, output filters, current control, and weak grids operation. *Energies, 16*(9), 3611. https://doi.org/10.3390/en16093611

DOI: 10.54254/2755-2721/2026.CH38770

[10] National Renewable Energy Laboratory. (2024). PVWatts calculator / PVWatts version 8. *NREL*.
[11] Kedika, N. R., & Salkuti, S. R. (2022). Enhanced maximum power point techniques for solar photovoltaic system under uniform insolation and partial shading conditions: A review. *Algorithms, 15*(10), 365. https://doi.org/10.3390/a15100365
[12] Adamas-Pérez, H., Ponce-Silva, M., Mina-Antonio, J. D., Claudio-Sánchez, A., Rodríguez-Benítez, O., & Rodríguez-Benítez, O. M. (2024). A new LCL filter design method for single-phase photovoltaic systems connected to the grid via micro-inverters. *Technologies, 12*(6), 89. https://doi.org/10.3390/technologies12060089
[13] Zhao, T., Li, J., & Gao, N. (2022). Capacitor-current-feedback with improved delay compensation for LCL-type grid-connected inverter to achieve high robustness in weak grid. *IEEE Access, 10*, 127956–127968. https://doi.org/10.1109/ACCESS.2022.3227391
[14] Li, S., & Lin, H. (2023). Passivity enhancement-based general design of capacitor current active damping for LCL-type grid-tied inverter. *IEEE Transactions on Power Electronics*. https://doi.org/10.1109/TPEL.2023.3265630